FULL PAPER

Silk Biomaterials with Vascularization Capacity

Hongyan Han, Hongyan Ning, Shanshan Liu, Qiang Lu,* Zhihai Fan, Haijun Lu, Guozhong Lu,* and David L. Kaplan

Functional vascularization is critical for the clinical regeneration of complex tissues such as kidney, liver, or bone. The immobilization or delivery of growth factors has been explored to improve vascularization capacity of tissue-engineered constructs; however, the use of growth factors has inherent problems such as the loss of signaling capability and the risk of complications including immunological responses and cancer. Here, a new method of preparing water-insoluble silk protein scaffolds with vascularization capacity using an all-aqueous process is reported. Acid is added temporally to tune the self-assembly of silk in the lyophilization process, resulting in water-insoluble scaffold formation directly. These biomaterials are mainly noncrystalline, offering improved cell proliferation than previously reported silk materials. These systems also have an appropriate softer mechanical property that could provide physical cues to promote cell differentiation into endothelial cells, and enhance neovascularization and tissue ingrowth in vivo without the addition of growth factors. Therefore, silk-based degradable scaffolds represent an exciting biomaterial option, with vascularization capacity for soft tissue engineering and regenerative medicine.

Prof. H. Han, H. Ning, Dr. S. Liu
National Engineering Laboratory for Modern
Silk & Collaborative Innovation Center
of Suzhou Nano Science and Technology
College of Textile and Clothing Engineering
Soochow University
Suzhou 215123, P. R. China

Prof. H. Han, H. Ning
School of Biology and Basic Medical Sciences
Soochow University
Suzhou 215123, P. R. China

Prof. Q. Lu, Prof. D. L. Kaplan
National Engineering Laboratory for Modern Silk
College of Textile and Clothing Engineering
Soochow University
Suzhou 215123, P. R. China
E-mail: Lvqiang78@suda.edu.cn

Dr. Z. Fan, H. Lu
Department of Orthopedics
The Second Affiliated Hospital of Soochow University
Suzhou 215000, P. R. China

Prof. G. Lu
Department of Burns and Plastic Surgery
The Third Affiliated Hospital of Nantong University
Wuxi 214041, P. R. China
E-mail: Luguozhong@hotmail.com

Prof. D. L. Kaplan
Department of Biomedical Engineering
Tufts University
Medford, MA 02155, USA

1. Introduction

Tissue engineering is a promising approach to regenerate damaged tissues and organs. However, only thin constructs such as skin and cartilage[1–3] have been successful, but fail when used to engineer thicker complex organs and tissues that require functional vasculature.[4–9] Thus, the incorporation of vascularization into biomaterial scaffolds remains a crucial challenge for the success of many tissue engineering strategies.

Blood vessels are formed by endothelial cell transformations that are regulated by dynamic interactions between endothelial cells, matrix factors, and growth factors.[10,11] The delivery of growth factors such as VEGF has been used to improve vascular perfusion in engineered scaffolds.[1,12] However, the rapid degradation of these factors remains a problem.[1,13] Although several conjugation methods have been developed to link VEGF to scaffolds to prolong bioavailability, the reaction conditions and cross-linking usually result in the denaturation of the protein, compromising cell-signaling capability.[1] Recently, the role of mechanics of scaffolds and the role of the ECM stiffness in cell differentiation have been considered.[14–17] The differentiation of stem cells to endothelial cells was achieved on materials with suitable stiffness, suggesting the possibility of designing biomaterial scaffolds with vascularization capacity through tuning scaffold stiffness.

Silk, a fibrillar protein, has been used in cell-support matrices for stem cells, nerve cells, fibroblasts and osteoblasts, and in scaffolds for skin, nerve, bone, cartilage, and blood vessel tissue engineering due to its impressive biocompatibility, unique mechanical properties, tunable biodegradability, and minimal inflammatory reactions.[18–26] The biocompatibility of silk scaffolds was further improved through fabricating silk nanostructures in lyophilization process.[27,28] However, treatments are usually required to achieve water insolubility of silk-based biomaterials, accompanied by high β-sheet structure formation,[29–31] which results in a higher stiffness than that required for vascularization.[30,31] Therefore, the fabrication of silk scaffolds with improved vascularization capacity remains a challenge because of the dilemma between achieving water-stability and the proper mechanical properties.

Recently, we reported a self-assembly mechanism to control silk nanostructures and conformations in aqueous solution.[32,33]

The mechanism suggested strong hydrophilic interactions endowed silk with improved stability, implying the possibility to prepare water insoluble silk scaffolds with reduced beta-sheet (crystalline) structure and thus softer mechanical properties.[34] Based on the assembly mechanism, water-dispersible silk nanofibers composed of β-sheet structures were prepared in our recent study and used to induce further nanofiber formation in a lyophilization process.[27] Here we developed a synergistic strategy to control the nanostructure and secondary conformation of silk scaffolds. The water-dispersible silk nanofibers were used to promote the conversion of silk in random secondary structures into nanofibers, while the pH of the silk solution was adjusted to eliminate the charge repulsion in order to achieve stronger hydrophilic interactions. Through tuning these two factors, water-insoluble silk scaffolds with reduced crystal structure were prepared directly without further posttreatment. Unlike the scaffolds reported previously,[29–31,35] these new water-insoluble nanofibrous scaffolds were mainly composed of random/silk I structure, providing softer mechanical property and vascularization capacity. The goal of the present study was to exploit this process to generate growth factor-free silk scaffold systems for vascularization needs.

2. Results and Discussion

2.1. Scaffold Structure Characterization

Nanofiber-assisting lyophilization can be used to improve porous structure formation in silk scaffolds.[36,37] Water-dispersible silk nanofibers prepared via controlled self-assembly were homogeneously blended with fresh silk solution to prepare microporous scaffolds with a lyophilization process. When the nanofiber content was above 6%, silk scaffolds with microporous structures were achieved and then became insoluble following achieving a pH to the isoelectric point, resulting in the direct preparation of water-insoluble scaffolds (Figure S1, Supporting Information). The microstructure of the scaffolds was revealed with scanning electron microscopy (SEM) (**Figure 1**). The scaffolds showed interconnected porous structures, but had
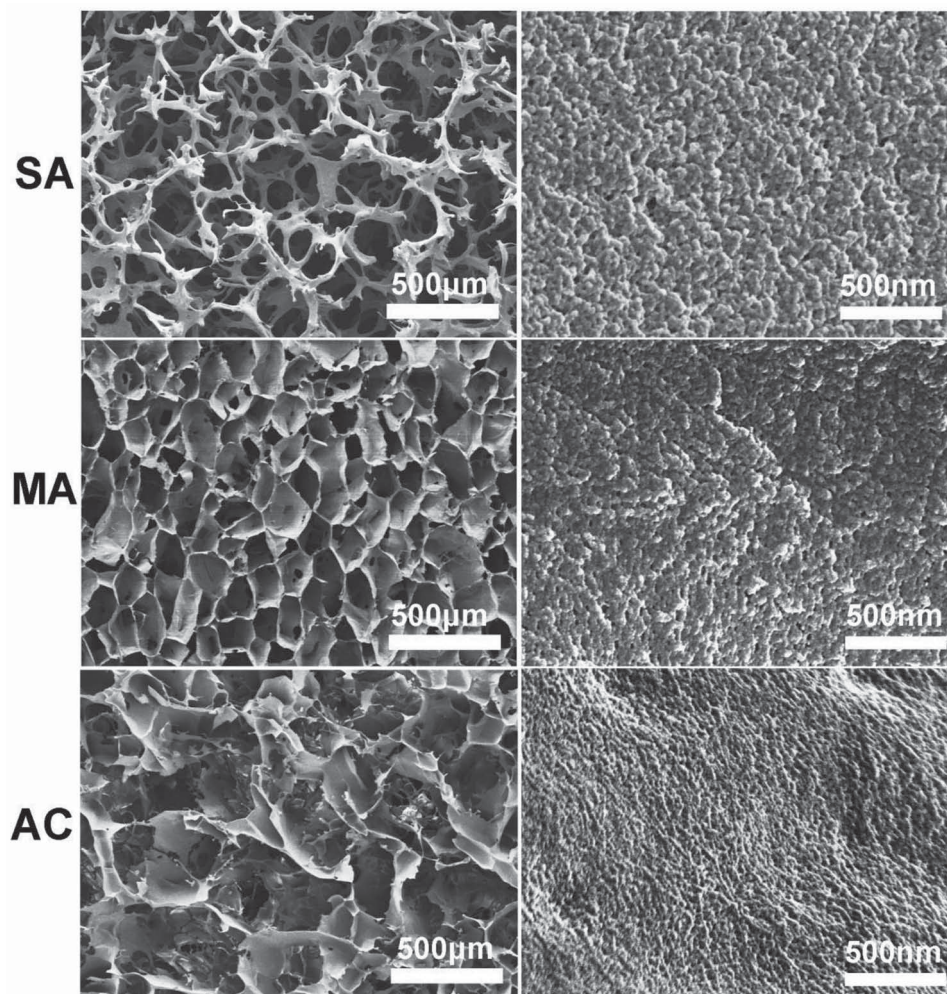
Figure 1. SEM morphologies of silk scaffolds prepared through different processes: The samples were as follows: SA, silk scaffolds prepared by salt-leaching process; MA, methanol-treated silk scaffolds derived from silk solution with 6.7% silk nanofiber; AC, acid-assisted silk scaffolds derived from silk solution with 6.7% silk nanofiber. The images on the right side show the nanoscaled topography of the pore wall with high magnification.

www.MaterialsViews.com

ADVANCED
FUNCTIONAL
MATERIALS
www.afm-journal.de

FULL PAPER
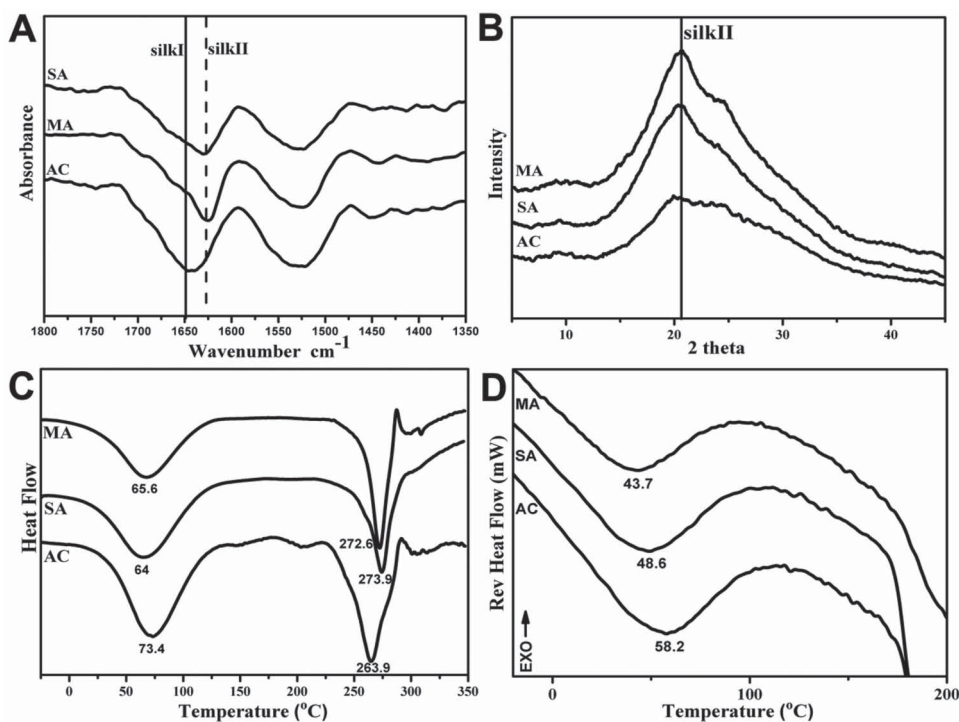
Figure 2. A) FTIR, B) XRD, C) DSC, and D) TMDSC characterization of silk scaffolds prepared through different processes: The samples were as follows: SA, silk scaffolds prepared by salt-leaching process; MA, methanol-treated silk scaffolds derived from silk solution with 6.7% silk nanofiber; AC, acid-assisted silk scaffolds derived from silk solution with 6.7% silk nanofiber.

various nanotopographies. The same amount of silk nanofibers as well as the same lyophilization process were performed for methanol-treated and acid-assisted scaffolds (MA and AC). However, nanoparticle topography appeared on the pore surface of salt-leached and methanol-treated scaffolds (SA and MA), but changed to nanofiber structures for the acid-assisted scaffolds (AC). This difference suggested that the adjustment of the pH changed the interactions between silk molecules and further induced nanofiber formation on the pore surfaces. The impact of topographical cues such as nanofibers, nanopores, and nanocolumns on cellular performance has been clarified in previous studies.[26–29] The ECM-mimetic nanofibrous structure was considered favorable for cell growth.[37–40] Therefore, unlike previous silk scaffolds, the nanofibers were exposed on the pore surfaces in the present study, to supply cues for cell adhesion and growth.[34,37]
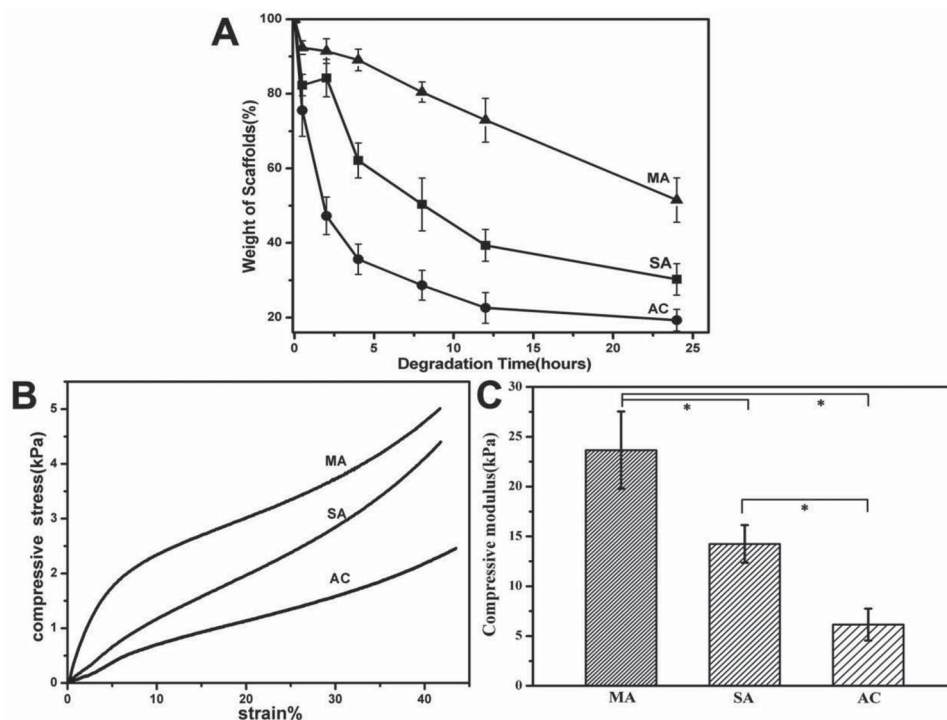
Structural changes of the silk scaffolds were investigated by Fourier transform infrared spectroscopy (FTIR) (**Figure 2**A). The infrared spectral region within 1700–1600 cm^{-1}, assigned to absorption by the peptide chains of amide I, is usually used for the analysis of different secondary structures of silk. The peaks at 1648–1652 cm^{-1} and 1635–1645 cm^{-1} are indicative of the silk I conformation and random coil, respectively, while the peaks at 1610–1630 cm^{-1} are characteristic of silk II conformation.[27,29,32,37] As shown in Figure 2A and Table S1 (Supporting Information), the salt-leached scaffolds (SA) and methanol-annealed scaffolds (MA) showed a main peak at 1628 cm^{-1}, while the acid-assisted scaffolds (AC) had strong peaks at 1640 and 1652 cm^{-1}. The results suggested that the amorphous states maintained in water-insoluble acid-assisted

scaffolds were significantly different when compared to previously reported scaffolds with high beta-sheet contents (MA and SA).[29–31,35] X-ray diffraction (XRD) curves further confirmed the lower beta-sheet content in the AC scaffolds (Figure 2B). Unlike the MA and SA scaffolds, the broader peaks between 10° and 35° appeared in the XRD curves of AC scaffolds, suggesting lower crystalline structure.[32,37,41] The crystal structures as well as the hydrophilic interactions of silk were further investigated by DSC. Figure 2C illustrates standard differential scanning calorimetry (DSC) curves for MA, SA, and AC scaffolds. All the scaffolds showed an endothermic peak at 50–100 °C and a degradation peak at 250–280 °C. Compared to MA and SA scaffolds, an endothermic peak at higher temperature and degradation peak at lower temperature appeared in the curve of the AC scaffolds, suggesting stronger hydrophilic interactions and an amorphous state. A higher endothermic peak also appeared in the temperature-modulated differential scanning calorimetry (TMDSC) curve of the AC scaffolds, further confirming the stronger hydrophilic interactions (Figure 2D). FTIR, XRD, and DSC results suggested that the water-insoluble AC scaffolds were mainly composed of amorphous structures, leading to softer mechanical properties and improved cell compatibility, based on previous studies.[34,37]

2.2. Scaffold Properties

The different secondary compositions resulted in different degradation rates (**Figure 3**A). Scaffolds degraded more quickly with decreased β-sheet content, as shown previously.[42] After

ADVANCED
FUNCTIONAL
MATERIALS
www.afm-journal.de

Materials
Views
www.MaterialsViews.com

Figure 3. A) Enzyme degradation and B,C) mechanical properties of silk scaffolds prepared through different processes. The samples were as follows: SA, silk scaffolds prepared by salt-leaching process; MA, methanol-treated silk scaffolds derived from silk solution with 6.7% silk nanofiber; AC, acid-assisted silk scaffolds derived from silk solution with 6.7% silk nanofiber. In enzyme degradation process, the samples were cultured in protease XIV solution (5 U mL^{-1} in PBS) at 37 °C. B) Typical stress–strain curves and C) compressive modulus of the scaffolds were measured in wet conditions.

exposure to protease XIV solution for 24 h, the AC scaffolds lost about 80% of their original weight, while the MA and SA scaffolds maintained 70% and 50% of their original weight, respectively. Figure 3B,C shows the mechanical properties of the different scaffolds. As expected, the AC scaffolds achieved softer mechanical properties due to the amorphous structure. The compressive modulus was about 6 kPa, significantly lower than that of MA and SA scaffolds (24 and 14 kPa, respectively). Different studies have revealed the influence of matrix elasticity on the differentiation of bone marrow mesenchymal stem cells (BMSC),[15,43,44] suggesting that an elastic modulus of 1–7 kPa facilitates the differentiation of BMSC into endothelial cells.[44,45] Therefore, the AC scaffolds had potential to induce the differentiation of stem cells into endothelial cells, providing a favorable microenvironment for vascularization, followed by regeneration of thicker tissues or organs.
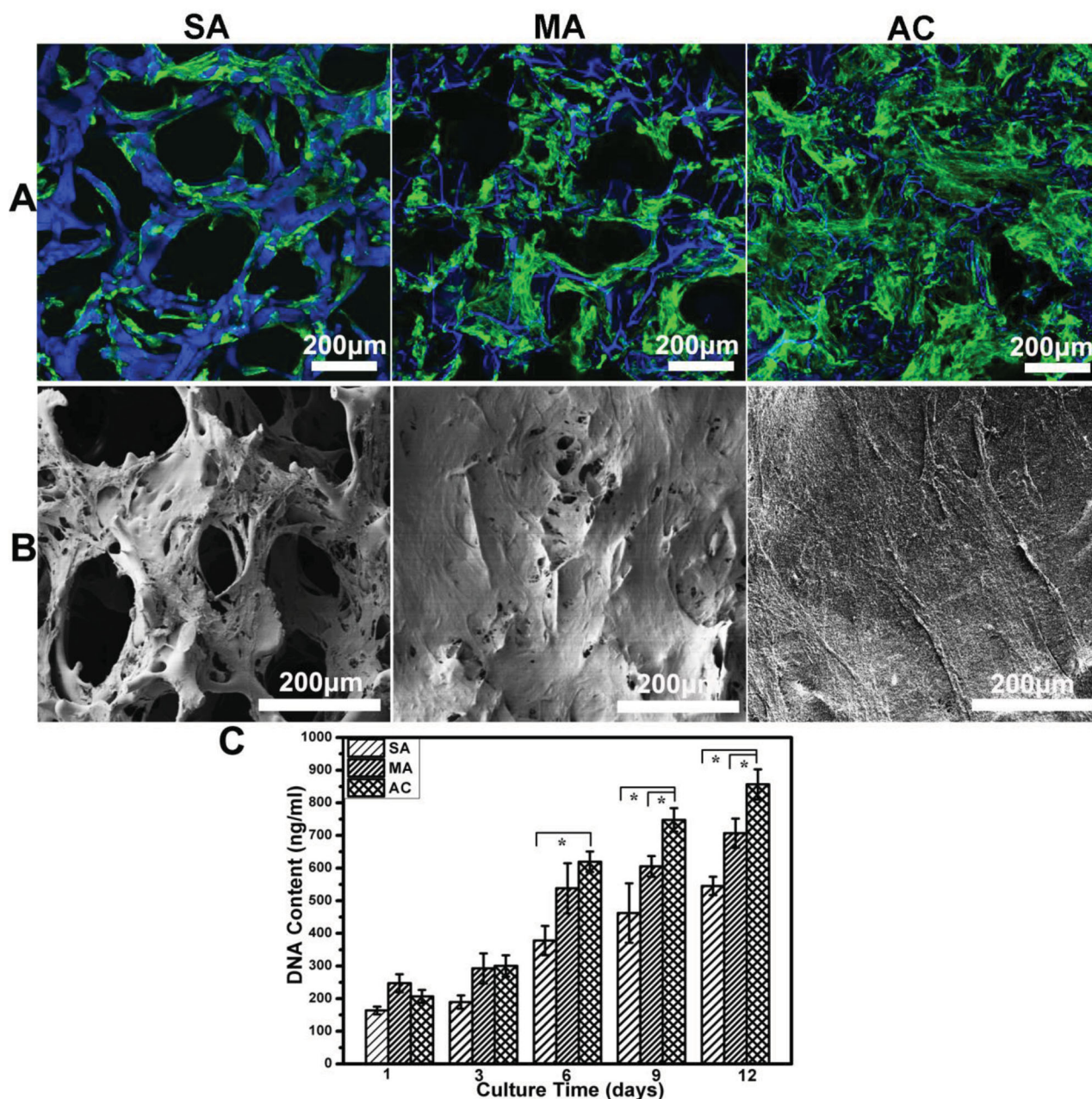
2.3. In Vitro Biocompatibility

BMSC attachment and proliferation were used to evaluate cell responses on the scaffolds. DNA content showed different cell proliferation behavior on the scaffolds (**Figure 4**). Cell numbers increased up to 12 d without reaching a plateau and higher cell numbers were achieved on the nanofibrous scaffolds (MA and AC). The nanofibrous scaffolds also showed a different cell proliferation behavior. BMSCs grew significantly better on the AC scaffolds than on the MA scaffolds. Previous studies revealed that both reduced β-sheet content and nanofibrous structures

of silk scaffolds resulted in improved cell compatibility.[37–40] DNA content suggested that the nanofibrous scaffolds, mainly composed of silk I/random structures, provided a better microenvironment for cell proliferation. Confocal microscopy and SEM results confirmed the improved cell growth on the AC scaffolds (Figures S2 and S3, Supporting Information). At day 12, cells proliferated and interacted to form more aggregates on the AC scaffolds than on the MA and SA scaffolds (Figure 4). More cell-ECM monolayer structures also formed on the AC scaffolds, implying better ECM formation. Therefore, in vitro cell cultures indicated that the nanofibrous silk scaffolds provided improved cell responses in vitro.

2.4. Endothelial Differentiation of BMSCs

Recent studies have demonstrated the effect of matrix stiffness on the differentiation of BMSCs.[15,46–48] In the present study, the modulus of the AC scaffolds was about 6 kPa. The data suggested the possibility of actively inducing the differentiation of stem cells to endothelial cells on the AC scaffolds.[44,45,49,50] The endothelial differentiation of BMSCs was studied with immunofluorescent staining of CD31 and key endothelial markers (KDR) (**Figure 5**).[46,51,52] Unlike the results found with the MA and SA scaffolds, significantly higher expression of KDR appeared on the AC scaffolds, following immunofluorescent staining of CD31 associated with vascular endothelial cells (Figure 5A,C).[51,52] The western blot was then used to quantify the CD31 production (Figure 5B), which also showed significant

Materials
Views
www.MaterialsViews.com

ADVANCED
FUNCTIONAL
MATERIALS
www.afm-journal.de

FULL PAPER

Figure 4. The proliferation behavior of BMSCs on different silk scaffolds: A) Fluorescence microscopy images of BMSC cultured on the samples at day 12, blue (DAPI) for nuclei and silk fibroin scaffolds; green (FITC labeled phalloidin) for F-actin; B) SEM images of BMSCs on the samples at day 12; C) BMSC proliferation on the samples measured with DNA analysis. *Statistically significant $P < 0.05$. The samples were as follows: SA, silk scaffolds prepared by salt-leaching process; MA, methanol-treated silk scaffolds derived from silk solution with 6.7% silk nanofiber; AC, acid-assisted silk scaffolds derived from silk solution with 6.7% silk nanofiber.

higher expression on the AC scaffolds. These results indicated that silk scaffolds with improved endothelial differentiation capacity could be achieved by the acid-assisted lyophilization process. In order to exclude the influence of nanostructure features on cell differentiation, the silk scaffolds (SCA), having similar nanofibrous structures but higher stiffness, (12.5 kPa) were prepared via a modified salt-leached method (Figure S4, Supporting Information). The stem cells on the SCA scaffolds didn't show differentiation into endothelial cells, confirming

the critical function of mechanical properties in inducing the differentiation into endothelial cells (Figure 5A).

2.5. In Vivo Vascularization Promoted by Mechanical Cues of Silk Scaffolds

Vascularization is essential for repairing damaged tissues since it provides enhanced nutrition, oxygen, and immune
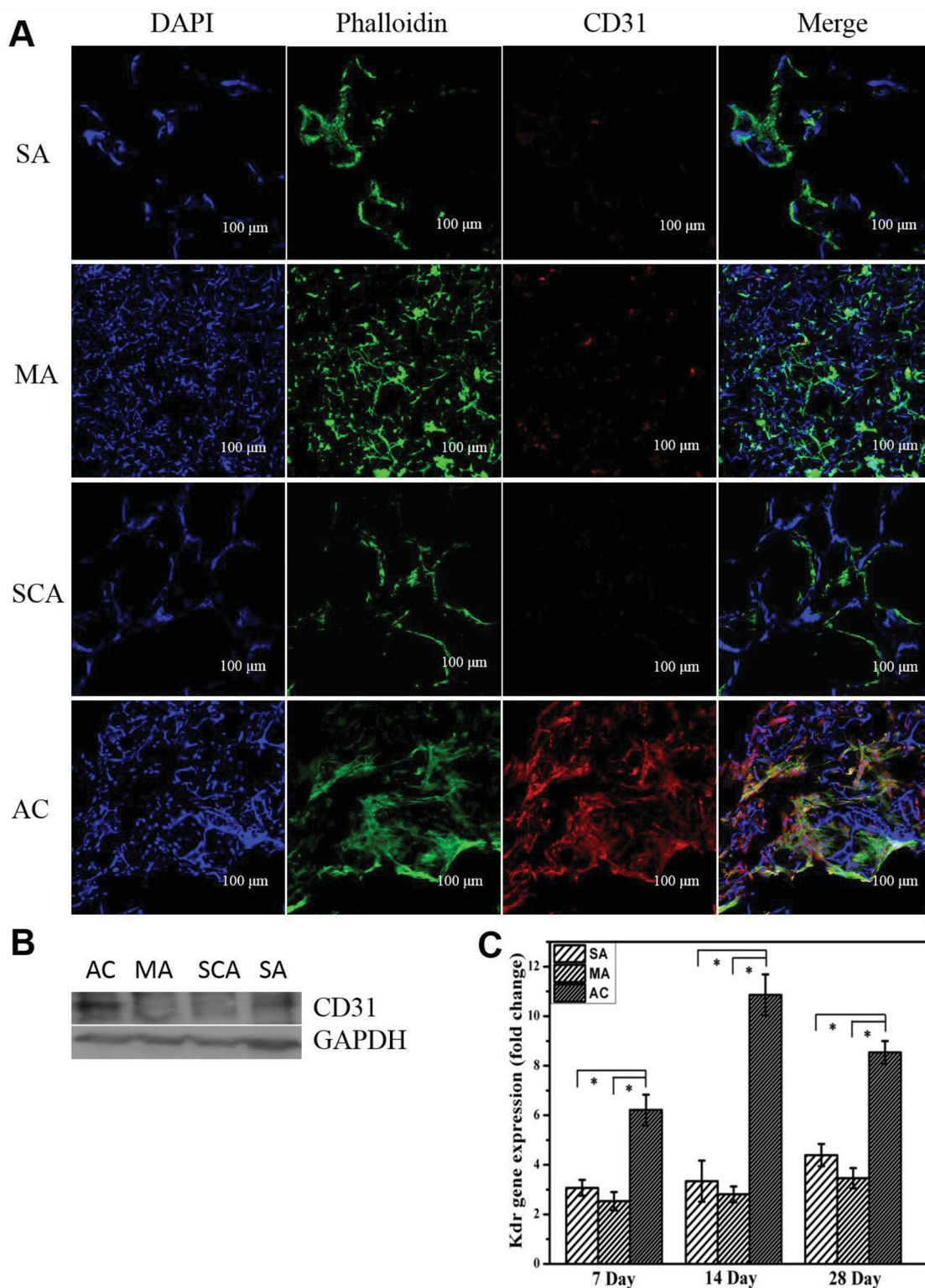
Figure 5. BMSC differentiation into endothelial cells on different silk scaffolds: A) the expression of CD31 (red) in different scaffolds at day 28 by confocal microscopy, blue (DAPI) for nuclei and silk fibroin scaffolds, green (FITC labeled phalloidin) for F-actin; B) the expression of CD31 at day 28 detected by western blot; C) mRNA levels of KDR quantified by real-time PCR. The samples were as follows: SA, silk scaffolds prepared by salt-leaching process; MA, methanol-treated silk scaffolds derived from silk solution with 6.7% silk nanofiber; SAC, silk scaffolds prepared by an acid-assisted salt-leaching process; AC, acid-assisted silk scaffolds derived from silk solution with 6.7% silk nanofiber. The expression of KDR is normalized to GAPDH. *Statistically significant $P < 0.05$.
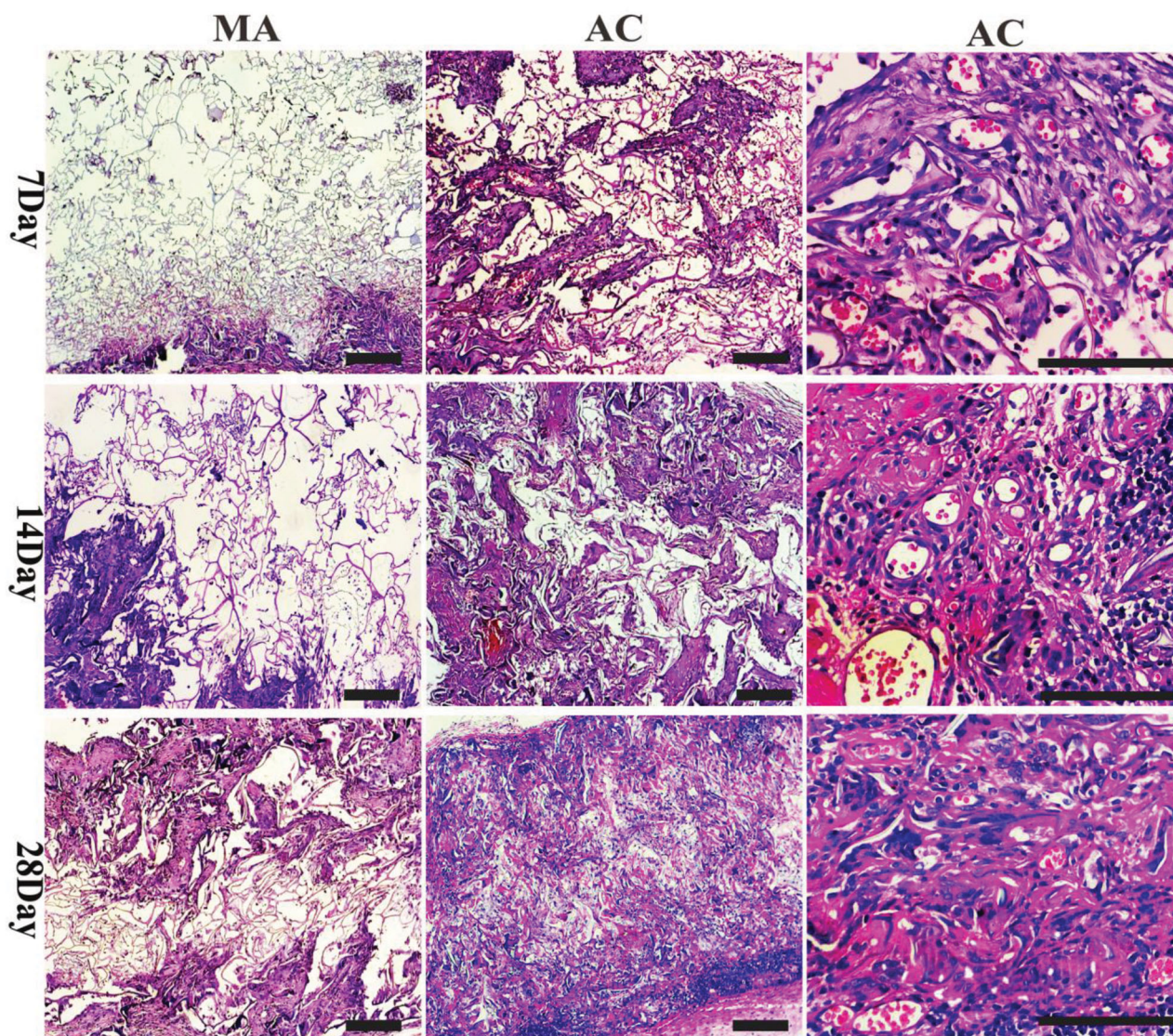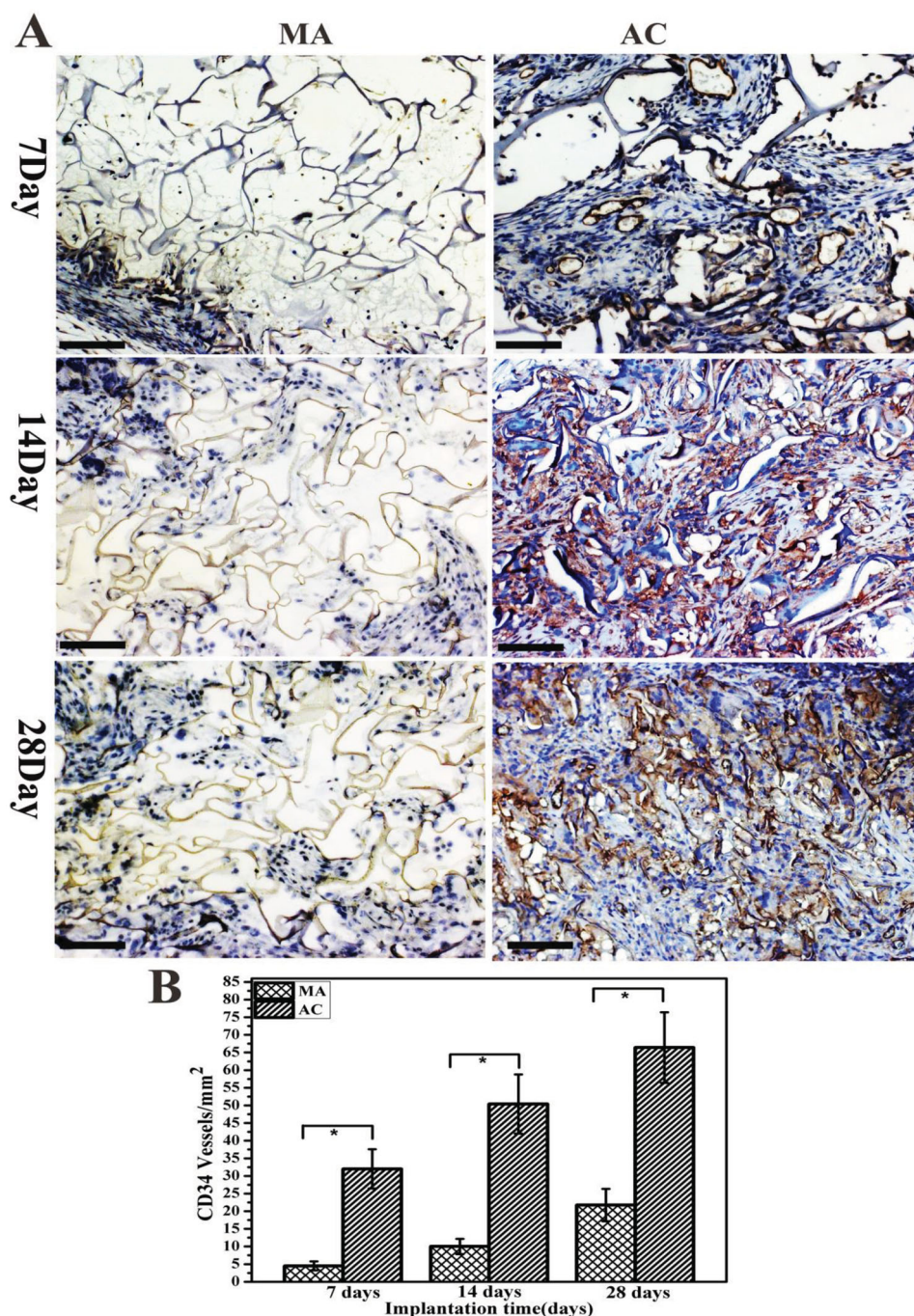
Figure 6. HE staining images of sections of AC and MA implants at 7, 14, and 28 d after implantation in vivo. Representative section images revealed better neovascularization and tissue ingrowth in AC implant. The right and middle pictures were the low magnification morphology of MA and AC samples (scale bar = 200 μm), while the right pictures showed the AC morphology at high magnification (scale bar = 100 μm). Protoplasm stained with picrosirius red and nuclei stained with blue.

cell transport to maintain the engineered tissue.[1,4] Various scaffolds and hydrogels have been reported to promote vascularization and tissue ingrowth mainly through cross-linking/encapsulating growth factors or active peptides.[1,53] To further evaluate the effects of mechanical induction of silk scaffolds on vascularization in vivo, the AC scaffolds were implanted subcutaneously in rats. The MA scaffolds with similar microstructure, but different stiffness, were used as a control. **Figures 6** and **7** show the histology of tissue sections and immunohistochemistry analysis for the AC and MA scaffolds. Significantly, more vasculatures in the scaffolds were observed visually in the AC at 7 d after implantation, but not in the MA after 7 d. Only few vasculatures could be found in the MA even after 14 d. By 28 d, significantly better vascularization was found in AC scaffolds, suggesting an accelerated neovascularization process.

The number of the formed vessels inside the scaffolds was also quantified (Figure 7). About 32 ± 5.6 vessels per mm^2 formed during the first week and increased to about 66 ± 10 vessels per mm^2 after four weeks in the AC scaffolds, while only 21.8 ± 3.6 blood vessels per mm^2 formed in the MA scaffolds at 28 d, confirming the vascularization capacity of the AC scaffolds. The vascularization in the AC scaffolds also seems better than that happened in VEGF-loaded silk scaffolds and other VEGF-loaded materials,[1,54–56] which would be further investigated in the following study.

The critical function of vascularization for the survival of cells and the transport of signaling molecules also resulted in different tissue regeneration behavior in the AC and MA scaffolds (Figures 6 and **Figure 8**). Since few blood vessels formed inside the MA scaffolds, new granulation tissue only slowly formed from

Figure 7. A) Immunohistochemistry staining images of sections of AC and MA implants at 7, 14, and 28 d after implantation in vivo (scale bar = 200 μm). The microvessels were stained with dark gray positive for CD34, and nuclei was stained with blue. B) Vessel density within the AC and MA scaffolds after implantation into the lateral incisions on the dorsal region. *Statistically significant $P < 0.05$.

outside to the interior. At 28 d after implantation, only about 60% of the MA scaffolds was overtaken by tissue ingrowth. Interestingly, blood vessels appeared in the interior of the AC scaffolds at 7 d after implantation, making the survival of cells feasible inside the AC scaffolds. Granulation tissue proceeded inside the AC scaffolds after one week and occupied about 85% of the scaffolds at 14 d. By 28 d, the scaffolds had been almost overtaken by

tissue ingrowth, further implicating the vascularization capacity of the AC scaffolds in promoting tissue regeneration. Compared to previously reported silk biomaterials,[13,35] our findings indicated that the water-insoluble silk scaffolds provided physical signals that directed stem cell differentiation into endothelial cells and vascular ingrowth. This new silk scaffold system with softer stiffness offered a simple, stable and effective means to design

www.MaterialsViews.com

ADVANCED
FUNCTIONAL
MATERIALS
www.afm-journal.de

FULL PAPER
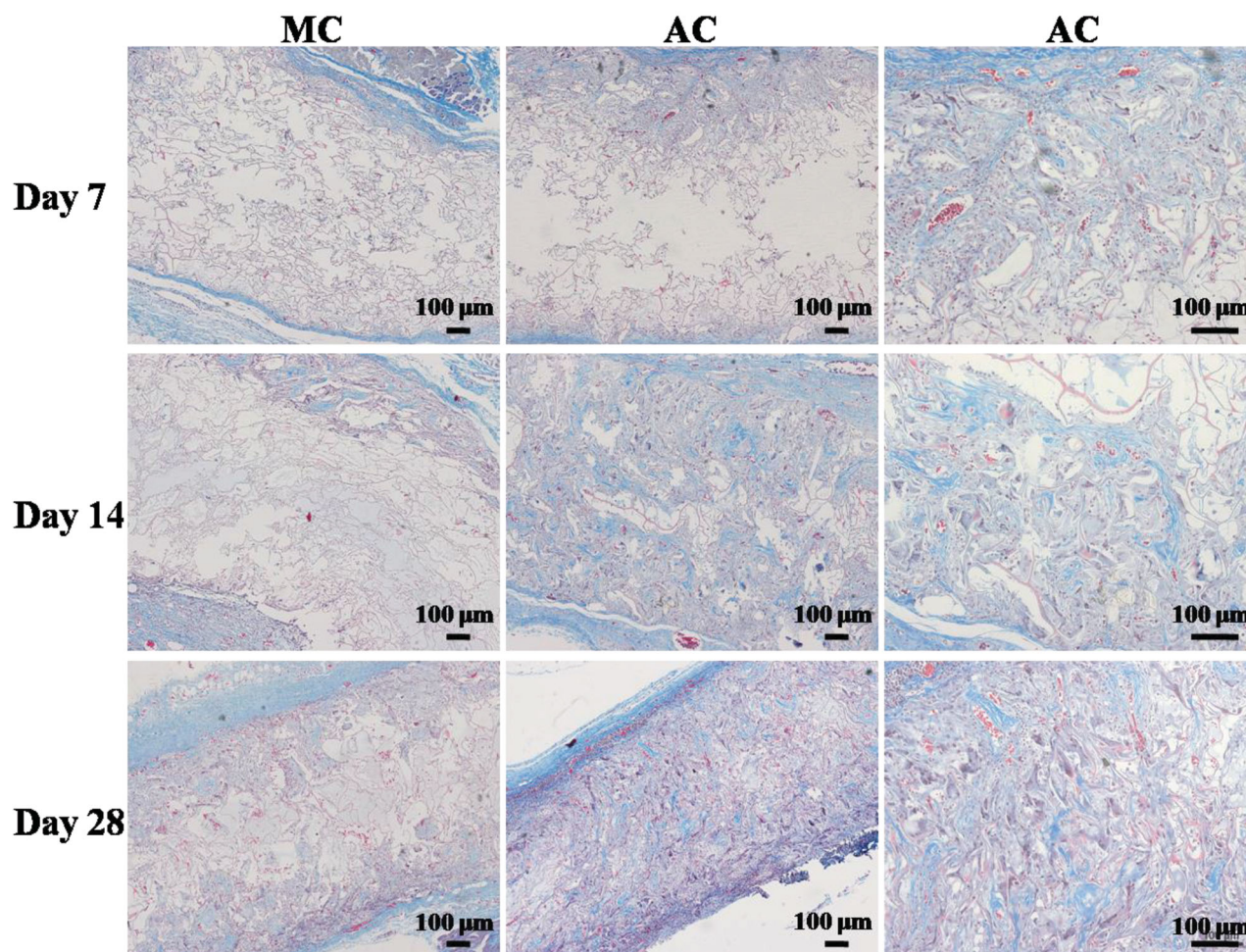
Figure 8. Masson trichrome staining images of sections of AC and MA implants at 7, 14 and 28 d after implantation in vivo. Collagen fibers are stained blue, nuclei are stained dark red/purple, and cytoplasm is stained pink.

soft tissue constructs with enhanced vascularization, without the use of metastable growth factors and peptides.

engineering of more natural and functional thick complex soft tissues.

3. Conclusions

The present work demonstrates a new strategy for designing natural, biocompatible, biodegradable, soft tissue matrices with vascularization capacity without the use of growth factors. The silk scaffolds were mainly composed of amorphous states and have a suitable stiffness to provide physical cues for vascularization. The improved stem cell proliferation and differentiation ability into endothelial cells, the strong neovascularization response in vivo, and the excellent tissue ingrowth capacity in vivo suggest that these should be promising scaffolds for soft tissue engineering. Additionally, the all-aqueous processing makes the process amenable to the incorporation of other ECM proteins, increasing the versatility of this new biomaterial. This unique combination of characteristics in a protein based scaffold without growth factors eliminates many of the disadvantages inherent in current biomaterials systems with vascularization capacity, which will allow the

4. Experimental Section

Animals: Female Sprague–Dawley (SD) rats, weighting 200 ± 50 g, were supplied by Laboratory Animal Research Center of Soochow University (Suzhou, China). All animal procedures followed the ethical guidelines of the experimental animals approved by Institutional Animal Care and Use Committee, Soochow University.

Preparation of Silk Solutions: B. mori silk solutions were prepared according to our previous published procedures.[36] Cocoons were boiled for 20 min in an aqueous solution of 0.02 M Na_2CO_3 and then rinsed thoroughly with distilled water to extract the sericin proteins. After drying, the extracted silk was dissolved in 9.3 M LiBr solution at 60 °C for 4 h, yielding a 20% (w/v) solution. This solution was dialyzed against distilled water using dialysis tube (molecular weight cut-off: 3500) for 72 h to remove the salt. Then the solution was centrifuged at 9000 rpm for 20 min at 4 °C to remove silk aggregates formed during the process. The final concentration of silk was about 6 wt%, determined by weighing the remaining solid after drying at 60 °C. The fresh silk solution was then diluted to 2 wt% with distilled water for subsequent lyophilized scaffold preparation.

Preparation of Silk Nanofiber Solution: The silk nanofibers were assembled as reported in our recent study.[57] Fresh silk solution was treated by a concentration–dilution process. The solution (6 wt%) was slowly concentrated to about 20 wt% over 24 h at 60 °C to form metastable nanoparticles, and then diluted to 0.5 wt% with distilled water. The diluted silk solution was incubated for 24 h at 60 °C to induce nanofiber formation.

Preparation of Silk Porous Scaffolds: Silk scaffolds were prepared via a modified lyophilization method.[36–38] According to our previous study, silk nanofibers could induce further silk nanofiber conversion in fresh solution and then form microporous scaffolds after lyophilization. The fresh silk solution was blended with silk nanofibers at different dry weight ratios (silk:silk nanofiber) of 100:0, 98:2, 93.3:6.7, and 88.2:11.8, respectively, and then used to prepare freeze-dried scaffolds (Figure S1, Supporting Information). Since good porous structures formed when the content of silk nanofibers was above 6.7%, the dry weight ratio of fresh silk and silk nanofibers was fixed to 93.3:6.7 in the present study. Then the pH of the blended solution was adjusted to the isoelectric point of silk (pI = 3.8–3.9) to eliminate charge repulsion. Specifically, the blend solution at a dry weight ratio (silk:silk nanofiber) of 93.3:6.7 was diluted to 2% with distilled water, and then adjusted to pH 4.0 by addition of 0.1 M hydrochloric acid (HCl). The mixed solution was poured into cylindrically shaped containers and frozen at −20 °C for 24 h, and then lyophilized for about 72 h. After lyophilization, the dried scaffolds were immersed in distilled water to remove hydrochloric acid until the pH of distilled water stabilized to about 7 without further change. Then, the scaffolds were freeze-dried again for subsequent characterization and termed AC. As a control, silk scaffolds derived from the same silk/silk nanofiber blend solution without HCl were prepared via same lyophilization process and then stabilized with methanol treatment. The salt-leached scaffolds were also prepared according to procedures reported elsewhere.[29] The methanol-treated scaffolds and salt-leached scaffolds were termed MA and SA, respectively. In order to further clarify the influence of mechanical properties on cell differentiation behaviors, the silk scaffolds having similar nanofibrous structure but higher stiffness were prepared through a modified salt-leached process. The fresh silk solution (6 wt%) was concentrated to above 20 wt% at 60 °C within 24 h and then diluted to 6 wt%. The pH of the diluted solution was adjusted to the isoelectric point of silk (pI = 3.8–3.9) to eliminate charge repulsion and induce nanofiber formation (Figure S4, Supporting Information). Finally, the scaffolds were prepared according to procedures reported elsewhere and termed SCA.

SEM: The morphology of the scaffolds was observed using a scanning electron microscopy (SEM, Hitachi S-4800, Hitachi, Tokyo, Japan) at 3 kV. Samples were mounted on a copper plate and sputter-coated with gold prior to imaging.[37]

FTIR: FTIR analysis of silk scaffolds was performed with a Nicolet FTIR 5700 spectrometer (Thermo Scientific, FL, USA), equipped with a MIRacle attenuated total reflection (Ge crystal).[37] For each measurement, 64 scans were co-added with a resolution of 4 cm^{-1} with the wavenumber ranging from 400 to 4000 cm^{-1}. Fourier self-deconvolution (FSD) of the infrared spectra covering the amide I region (1595–1705 cm^{-1}) was performed using Peakfit software to identify silk secondary structures.[40]

XRD: The crystalline of the obtained scaffolds was measured with X-ray diffraction (XRD) (X´ Pert-Pro MPD, PANalytical BV, Almelo, Holland) using monochromated Cu Kα radiation (30 mA, 40 kV) with a scanning speed of 6° min^{-1}.[37]

DSC: The thermal properties of the scaffolds were measured in a Q 2000 DSC instrument (TA Company, New Castle, DE) under a dry nitrogen flow of 50 mL min^{-1}. TMDSC measurements were performed using a TA instrument Q2000 equipped with a refrigerated cooling system. The samples were heated at 2 °C min^{-1} with a modulation period of 60 s and a temperature amplitude of 0.318 °C.[29]

Enzyme Degradation: The scaffolds were incubated in protease XIV solution (5 U mL^{-1} in PBS) to evaluate degradation.[37] Samples were soaked in protease XIV solution at scaffold/solution weight ratios of 1:99 and then kept at 37 °C in a shaking water bath for 0.5, 2, 4, 8, 12,

and 24 h. At designated time points, five samples for each group were dried and weighed. The residual mass (%) was obtained by dividing residual weight by the initial weight. Five samples were carried out for each measurement.

Mechanical Properties: To measure the compressive properties of the scaffolds (11 mm in diameter and 22 mm in height) in hydrated conditions, the scaffolds were first hydrated in water for 4 h and then measured with a cross head speed of 2 mm min^{-1} at 25 °C using an Instron 3366 testing frame (Instron, Norwood, MA) with a 10 N loading cell.[4,38] The load was applied until the cylinder was compressed by more than 30% of its original length.[34] The compressive modulus was calculated as the slope of the linear-elastic region of the stress–strain curve. Five samples were carried out for each group.

In Vitro Biocompatibility of Scaffolds: BMSCs derived from SD rats were used to evaluate the in vitro biocompatibility of the scaffolds. The scaffolds were punched into small disks (diameter of 8 mm and height of 2 mm) for 96-well plates, and sterilized with ^{60}Co γ-irradiation at the dose of 50 kGy. BMSCs were cultured in Dulbecco's modified Eagle medium (DMEM, low glucose) supplemented with 10% fetal bovine serum (FBS), and 1% IU mL^{-1} streptomycin-penicillin (Invitrogen, Carlsbad, CA). After reaching 90% confluence, cells were detached from Petri dish and seeded into the scaffolds at a density of 1.0×10^5 cells per well.

The cell morphology on the scaffolds was examined by confocal microscopy. After culture for 1, 6, and 12 d, the cell-seeded scaffolds were washed three times with PBS and fixed in 4% paraformaldehyde (Sigma-Aldrich, St Louis, MO) for 30 min, followed by further washing. The cells were permeabilized with 0.1% Triton X-100 for 5 min and incubated with FITC-phalloidin (Sigma-Aldrich, St. Louis, MO) for 20 min at room temperature, followed by washing with PBS and, finally, staining with DAPI (Sigma-Aldrich, St. Louis, MO) for 1 min. Representative fluorescence images of the stained samples were obtained using a confocal microscope (Olympus FV10 inverted microscope, Nagano, Japan) with excitation/emission at 358/462 nm and 494/518 nm. The images of the scaffolds were captured from the surface to a depth of 100 μm in increments of 10 μm. The cell morphology on the scaffolds was confirmed by SEM. After harvest, the cell-seeded scaffolds were washed three times with PBS, fixed in 4% paraformaldehyde at room temperature, and then again washed three times with PBS. Fixed samples were dehydrated through a gradient of alcohol (50%, 70%, 80%, 90%, 100%, 100%) followed by lyophilization. After coated with gold, the samples were examined with SEM at the voltage of 10 kV. Several different areas of the specimens were randomly examined using a Hitachi model S-4800 scanning electron microscopy (Hitachi, Tokyo, Japan).

To study cell proliferation on the scaffolds, samples harvested at the indicated time points (from 1 to 12 d) were digested with proteinase K buffer solution for 16 h at 56 °C, as described previously.[37,38] The DNA content was determined using the PicoGreen DNA assay, following the protocol of the manufacturer (Invitrogen, Carlsbad, CA). Samples (n = 5) were measured at an excitation wavelength of 480 nm and emission wavelength of 530 nm, using a BioTeK Synergy 4 spectrofluorometer (BioTeK, Winooski, VT). The amount of DNA was calculated by interpolation from a standard curve prepared with λ-phage DNA in 10×10^{-3} M Tris-HCl (pH 7.4), 5×10^{-3} M NaCl, 0.1×10^{-3} M EDTA over a range of concentrations.

In Vitro Cell Differentiation on the Scaffolds: BMSCs derived from SD rats were used to evaluate the in vitro cell differentiation on the scaffolds. Cell differentiation was studied via quantitative real-time PCR (qRT-PCR) and immunofluorescence staining.[39,44]

Endothelial differentiation gene expression of BMSCs cultured on the scaffolds was evaluated by quantitative real-time PCR. On 1, 7, 14, and 28 d, the total cellular RNA from each sample was extracted with Trizol reagent (Invitrogen, Carlsbad, USA). RNA concentration in each sample was analyzed through measuring the optical density at 260 nm with a Nano Drop 2000 (Thermo Scientific, Waltham, MA). 1 μg of the extracted RNA was converted into complementary DNA (cDNA) using a High-Capacity cDNA Reverse Transcription kit (Applied Biosystems,

www.MaterialsViews.com

ADVANCED
FUNCTIONAL
MATERIALS
www.afm-journal.de

FULL PAPER

Table 1. Sequences of primers used in real-time PCR(PR-PCR).

Genes	Primer sequence (F, R, 5'-3')	Product length (bp)
GAPDH	TGGGTGTGAACCACGAGAA	143
	GGCATGGACTGTGGTCATGA	
KDR	CTGCCAGCTCAGGTTTTGTG	172
	AGGTCCCTGTGGATACACTTC	

Carlsbad, USA) in a 2720 thermal cycler (Applied Biosystems, Foster City, CA, USA). Quantitative real-time PCR was performed in a 7500 Real-Time PCR System (Applied Biosystems, Foster City, CA, USA) with the Fast SYBR Green kit (Applied Biosystems, Carlsbad, USA). The conditions for the PCR reaction were as follows: 95 °C (20 s), 40 cycles at 95 °C (3 s), and 60 °C (30 s). The sequence of primers is given in **Table 1**. The mRNA expression level was expressed as threshold cycle (CT) values, and the expression of the house keeping gene GAPDH was used as internal control to normalize results. The comparative Ct-value method was used to calculate the relative expression. Each sample was analyzed in triplicate.

Immunofluorescence Staining: Immunofluorescence staining of cells with CD31 (endothelial cell marker) was used to characterize endothelial differentiation of BMSCs.[13,51] Briefly, the samples were fixed in PBS containing 4% paraf maldehyde (Sigma-Aldrich, St. Louis, MO, USA) for 30 min, permeabilized with 1% Triton X-100 in PBS for 10 min, washed three times with PBS, and blocked in PBS containing 3% BSA for 1 h. Cells were incubated with anti-CD31 primary antibodies (Abcam, Cambridge, MA, USA) diluted in blocking buffer for 1 h. Samples were then rinsed three times with PBS containing 0.1% Tween-20 and incubated with secondary antibodies. DNA and silk scaffolds were identified by staining with DAPI (Sigma-Aldrich, St. Louis, MO, USA), FITC-phalloidin (Invitrogen, Grand Island, NY, USA) was used to stain F-actin. Representative fluorescence images of stained samples were obtained by confocal laser scanning microscopy (CLSM, Olympus FV10 inverted microscope, Nagano, Japan).

Western Blot: Samples were lysed in RIPA lysis buffer (50×10^{-3} M Tris-HCl, pH 7.4, 150×10^{-3} M NaCl, 1% NP-40, 0.1% SDS, and 0.5% sodium deoxycholate) containing 10 µg mL^{-1} aprotinin, 10 µg mL^{-1} leupeptin, and 1×10^{-3} M PMSF. Equal amounts of lysates were electrophoresed in 12% SDS-polyacrylamide gels, and proteins were transferred to a nitrocellulose membrane. Membranes were blocked with 5% defatted milk and probed with anti-CD31 antibodies, then incubated with secondary antibodies conjugated with horseradish peroxidase. The ECL western blotting analysis system was used to detect the substrates.

Subcutaneous Implantation: Animal ethics approval for the use of SD rats in this experiment was granted by the animal ethics committee of Soochow university. Each SD rat was subcutaneously implanted with scaffolds, $10 \times 10 \times 3$ mm in size, treated with methanol or acid, respectively. All scaffolds were sterilized and immersed in PBS for hours before the implantation and then implanted into lateral incisions on the dorsal region. Subcutaneous implantation in lateral pockets under general anesthesia of chloral hydrate.[13,35] At weeks 1, 2, and 4 postimplantation, animals were euthanized and the specimens along with the adjacent tissues were collected for further examinations.[53]

Histology and Immunohistochemistry: Samples were fixed with 10% neutral buffered formalin (NBF) at room temperature and embedded in paraffin after a series of xylene and graded ethanol washes. Samples were sectioned (5–6 µm thickness), deparaffinized, and stained with hematoxylin and eosin (H&E) (Sigma-Aldrich) to visualize cell nuclei and cytoplasm, respectively. In order to characterize lumen formation, sections were probed with primary antibody against the endothelial cell marker, CD34 (1:100 dilution, Abcam), followed by secondary antibody labeled with HRP (Horseradish peroxidase), and counterstained with hematoxylin using reagents from a Histostain-SP kit (Invitrogen). Vessels were counted under an inverted microscope (AxioVert A1, Carl Zeiss, Germany).[51] The vessels formed in the constructs in vivo

were quantified by evaluation of six random view fields (under 20× magnification) of the stained sections that came from three individual mice (two fields per mouse). The density of each vessel was reported as the average number of vessels and expressed as mean values ± the standard deviation.[34]

Masson Trichrome Staining: Slides were deparaffinized, rehydrated, and incubated in Weigert's iron hematoxylin working solution for 10 min, followed by Biebrich scarlet-acid fuchsin, phosphomolybdic/phosphotungstic acid solution, and aniline blue. Then, sections were dehydrated very quickly, cleared in xylene, and mounted with resinous mounting medium.

Statistical Methods: All statistical analyses were performed using SPSS v.16.0 software. Comparison of the mean values of the data sets was performed using one-way AVOVA. Measures are presented as means ± standard deviations, unless otherwise specified. $P < 0.05$ was considered significant.

Supporting Information

Supporting Information is available from the Wiley Online Library or from the author.

Acknowledgements

[1] P. J. Stahl, T. R. Chan, Y. I. Shen, G. Sun, S. Gerecht, S. M. Yu, *Adv. Funct. Mater.* **2014**, 24, 3213.

[2] J. Mansbridge, *J. Biomater. Sci.* **2008**, 19, 955.

[3] J. S. Temenoff, A. G. Mikos, *Biomaterials* **2000**, 21, 431.

[4] L. S. Wray, K. Tsioris, E. S. Gil, F. G. Omenetto, D. L. Kaplan, *Adv. Funct. Mater.* **2013**, 23, 3404.

[5] L. G. Griffith, G. Naughton, *Science* **2002**, 295, 1009.

[6] H. C. Ko, B. K. Milthorpe, C. D. McFarland, *Eur. Cells Mater.* **2007**, 14, 1.

[7] M. W. Laschke, Y. Harder, M. Amon, I. Martin, J. Farhadi, A. Ring, N. Torio-Padron, R. Schramm, M. Rucker, D. Junker, *Tissue Eng.* **2006**, 12, 2093.

[8] Z. Lokmic, G. M. Mitchell, *Tissue Eng. Part B* **2008**, 14, 87.

[9] J. Rouwkema, N. C. Rivron, C. A. van Blitterswijk, *Trends Biotechnol.* **2008**, 26, 434.

[10] A. Schmidt, K. Brixius, W. Bloch, *Circ. Res.* **2007**, 101, 125.

[11] M. E. Francis, S. Uriel, E. M. Brey, *Tissue Eng. Part B* **2008**, 14, 19.

[12] W. J. Zhang, C. Zhu, Y. Q. Wu, D. X. Ye, S. Y. Wang, D. H. Zou, X. L. Zhang, D. L. Kaplan, X. Q. Jiang, *Eur. Cells Mater.* **2014**, 27, 1.

[13] M. Stoppato, H. Y. Stevens, E. Carletti, C. Migliaresi, A. Motta, R. E. Guldberg, *Biomaterials* **2013**, 34, 4573.

[14] H. Sun, F. Zhu, Q. Hu, P. H. Krebsbach, *Biomaterials* **2014**, 35, 1176.

FULL PAPER

[15] A. J. Engler, S. Sen, H. L. Sweeney, D. E. Discher, *Cell* **2006**, *126*, 677.

[16] F. Guilak, D. M. Cohen, B. T. Estes, J. M. Gimble, W. Liedtke, C. S. Chen, *Cell Stem Cell* **2009**, *5*, 17.

[17] a) P. M. Gilbert, K. L. Havenstrite, K. E. G. Magnusson, A. Sacco, N. A. Leonardi, P. Kraft, N. K. Nguyen, S. Thrun, M. P. Lutolf, H. M. Blau, *Science* **2010**, *329*, 1078; b) G. H. Altman, F. Diaz, C. Jakuba, T. Calabro, R. L. Horan, J. Chen, H. Lu, J. Richmond, D. L. Kaplan, *Biomaterials* **2003**, *24*, 401.

[18] H. Liu, H. Fan, Y. Wang, S. L. Toh, J. C. H. Goh, *Biomaterials* **2008**, *29*, 662.

[19] D. Marolt, A. Augst, L. E. Freed, C. Vepari, R. Fajardo, N. Patel, M. Gray, M. Farley, D. Kaplan, G. Vunjak-Novakovic, *Biomaterials* **2006**, *27*, 6138.

[20] C. Vepari, D. L. Kaplan, *Prog. Polym. Sci.* **2007**, *32*, 991.

[21] Y. Zhang, W. Fan, Z. Ma, C. Wu, W. Fang, G. Liu, Y. Xiao, *Acta Biomater.* **2010**, *6*, 3021.

[22] J. L. Chen, Z. Yin, W. L. Shen, X. Chen, B. C. Heng, X. H. Zou, H. W. Ouyang, *Biomaterials* **2010**, *31*, 9438.

[23] K. Ziv, H. Nuhn, Y. Ben-Haim, L. S. Sasportas, P. J. Kempen, T. P. Niedringhaus, M. Hrynyk, R. Sinclair, A. E. Barron, S. S. Gambhir, *Biomaterials* **2014**, *35*, 3736.

[24] Q. Zhang, Y. Zhao, S. Yan, Y. Yang, H. Zhao, M. Li, S. Lu, D. L. Kaplan, *Acta Biomater.* **2012**, *8*, 2628.

[25] C. Correia, S. Bhumiratana, L. P. Yan, A. L. Oliveira, J. M. Gimble, D. Rockwood, D. L. Kaplan, R. A. Sousa, R. L. Reis, G. Vunjak-Novakovic, *Acta Biomater.* **2012**, *8*, 2483.

[26] S. Lin, G. Lu, S. Liu, S. Bai, X. Liu, Q. Lu, B. Zuo, D. L. Kaplan, H. Zhu, *J. Mater. Chem. B* **2014**, *2*, 2622.

[27] S. Liu, C. Dong, G. Lu, Q. Lu, Z. Li, D. L. Kaplan, H. Zhu, *Acta Biomater.* **2013**, *9*, 8991.

[28] D. Yao, S. Dong, Q. Lu, X. Hu, D. L. Kaplan, B. Zhang, H. Zhu, *Biomacromolecules* **2012**, *13*, 3723.

[29] U. J. Kim, J. Park, H. J. Kim, M. Wada, D. L. Kaplan, *Biomaterials* **2005**, *26*, 2775.

[30] R. Nazarov, H. J. Jin, D. L. Kaplan, *Biomacromolecules* **2004**, *5*, 718.

[31] Q. Lu, X. Wang, S. Lu, M. Li, D. L. Kaplan, H. Zhu, *Biomaterials* **2011**, *32*, 1059.

[32] Q. Lu, H. Zhu, C. Zhang, F. Zhang, B. Zhang, D. L. Kaplan, *Biomacromolecules* **2012**, *13*, 826.

[33] Y. Pei, X. Liu, S. Liu, Q. Lu, J. Liu, D. L. Kaplan, H. Zhu, *Acta Biomater.* **2015**, *13*, 168.

[34] L. Ren, Y. Kang, C. Browne, J. Bishop, Y. Yang, *Bone* **2014**, *64*, 173.

[35] S. Bai, S. Liu, C. Zhang, W. Xu, Q. Lu, H. Han, D. L. Kaplan, H. Zhu, *Acta Biomater.* **2013**, *9*, 7806.

[36] F. Han, S. Liu, X. Liu, Y. Pei, S. Bai, H. Zhao, Q. Lu, F. Ma, D. L. Kaplan, H. Zhu, *Acta Biomater.* **2014**, *10*, 921.

[37] G. Lu, S. Liu, S. Lin, D. L. Kaplan, Q. Lu, *Colloid Surf. B* **2014**, *120*, 28.

[38] X. Hu, S. H. Park, E. S. Gil, X. X. Xia, A. S. Weiss, D. L. Kaplan, *Biomaterials* **2011**, *32*, 8979.

[39] Q. Lu, X. Hu, X. Wang, J. A. Kluge, S. Lu, P. Cebe, D. L. Kaplan, *Acta Biomater.* **2010**, *6*, 1380.

[40] J. Zhu, Y. Zhang, H. Shao, X. Hu, *Polymer* **2008**, *49*, 2880.

[41] X. Hu, Q. Lu, D. L. Kaplan, P. Cebe, *Macromolecules* **2009**, *42*, 2079.

[42] N. D. Leipzig, M. S. Shoichet, *Biomaterials* **2009**, *30*, 6867.

[43] A. B. Mathur, A. M. Collinsworth, W. M. Reichert, W. E. Kraus, G. A. Truskey, *J. Biomech.* **2001**, *34*, 1545.

[44] K. Wingate, W. Bonani, Y. Tan, S. J. Bryant, W. Tan, *Acta Biomater.* **2012**, *8*, 1440.

[45] J. Zoldan, E. D. Karagiannis, C. Y. Lee, D. G. Anderson, R. Langer, S. Levenberg, *Biomaterials* **2011**, *32*, 9612.

[46] Y. S. Pek, A. C. A. Wan, J. Y. Ying, *Biomaterials* **2010**, *31*, 385.

[47] J. S. Park, J. S. Chu, A. D. Tsou, R. Diop, Z. Tang, A. Wang, S. Li, *Biomaterials* **2011**, *32*, 3921.

[48] S. Even-Ram, V. Artym, K. M. Yamada, *Cell* **2006**, *126*, 645.

[49] Y. Sun, L. G. Villa-Diaz, R. H. W. Lam, W. Chen, P. H. Krebsbach, J. Fu, *PLOS One* **2012**, *7*, 37178.

[50] M. T. Valarmathi, J. M. Davis, M. J. Yost, R. L. Goodwin, J. D. Potts, *Biomaterials* **2009**, *30*, 1098.

[51] N. F. Huang, J. Okogbaa, J. C. Lee, A. Jha, T. S. Zaitseva, M. V. Paukshto, J. S. Sun, N. Punjya, G. G. Fuller, J. P. Cooke, *Biomaterials* **2013**, *34*, 4038.

[52] B. P. Partlow, C. W. Hanna, J. Rnjak-Kovacina, J. E. Moreau, M. B Applegate, K. A. Burke, B. Marelli, A. N. Mitropoulos, F. G. Omenetto, D. L. Kaplan, *Adv. Funct. Mater.* **2014**, *24*, 4615.

[53] M. Zhu, K. Wang, J. Mei, C. Li, J. Zhang, W. Zheng, D. An, N. Xiao, Q. Zhao, D. Kong, L. Wang, *Acta Biomater.* **2014**, *10*, 2014.

[54] C. Bigalke, F. Luderer, K. Wulf, T. Storm, M. Löbler, D. Arbeiter, B. M. Rau, H. Nizze, B. Vollmar, K. P. Schmitz, E. Klar, K. Sternberg, *Acta Biomater.* **2014**, *10*, 5081.

[55] W. Zhang, X. Wang, S. Wang, J. Zhao, L. Xu, C. Zhu, D. Zeng, J. Chen, Z. Zhang, D. L. Kaplan, X. Jiang, *Biomaterials* **2011**, *32*, 9415.

[56] S. Bai, X. Zhang, Q. Lu, W. Sheng, L. Liu, B. Dong, D. L. Kaplan, H. Zhu, *Biomacromolecules* **2014**, *15*, 3044.

[57] I. Karakutuk, F. AK, O. Okay, *Biomacromolecules* **2012**, *13*, 1122.